International Journal of Heat and Technology
Vol. 43, No. 6, December, 2025, pp. 2173-2186
Journal homepage: http://iieta.org/journals/ijht

Cross-Scale Coupling Effects of Urban Block Wind Fields on Indoor Luminous–Thermal Environments of Buildings

Sufang Liu[1*], Dong Yan[1], Chuan Wang[1], Hang He[1], Senmiao Yang[2]

[1] College of Architecture, Nanyang Institute of Technology, Nanyang 473000, China
[2] Nanyang No.1 High School, Nanyang 473000, China

Corresponding Author Email: 3062011@nyist.edu.cn

https://doi.org/10.18280/ijht.430617

Received: 28 March 2025
Revised: 16 October 2025
Accepted: 1 November 2025
Available online: 31 December 2025

Keywords:
cross-scale thermodynamic coupling, data assimilation, indoor luminous–thermal environment, wind-field-mediated energy transfer, entropy production minimization, uncertainty quantification

ABSTRACT

High-density urban development has induced pronounced non-equilibrium thermodynamic characteristics in block-scale microclimates. During the cross-scale coupling between urban wind fields and indoor luminous–thermal environments of buildings, fundamental challenges persist, including spatiotemporal heterogeneity of multiscale processes, discontinuities in energy transfer, and the lack of thermodynamic consistency. These issues significantly constrain the synergistic optimization of indoor thermal comfort and building energy efficiency. To accurately characterize this cross-scale coupling mechanism, this study proposes a thermodynamically consistent cross-scale dynamic coupling simulation framework, termed DA-PG-CSDC. The framework integrates data assimilation with physics-guided generative models, embedding non-equilibrium thermodynamic constraints and entropy flow–entropy production analysis. Through the coordinated design of dynamic correction, physical downscaling, and bidirectional coupling, the framework enables full-process quantification of cross-scale energy transfer and dissipation. Experimental validation demonstrates that the DA-PG-CSDC framework achieves excellent thermodynamic consistency and predictive accuracy, with an energy balance error of no more than 2.3% and a mean absolute temperature prediction error within 0.8℃. In scaled experiments, deviations in temperature and heat flux density simulations are limited to 1.1℃ and 5.0%, respectively. Application results indicate that optimized wind fields can reduce the indoor average temperature by 1.8℃, decrease the total system entropy production rate by 20.7%, and lower building air-conditioning energy consumption by 17.5%. Uncertainty analysis further identifies computational fluid dynamics (CFD) turbulence model constants as key influencing factors. The proposed coupling framework provides a novel methodological paradigm for cross-scale non-equilibrium thermodynamic analysis and offers strong theoretical support and engineering applicability for optimizing indoor luminous–thermal environments and advancing low-carbon building design.

1. INTRODUCTION

The changes in underlying surfaces induced by high-density urban development have led to pronounced non-equilibrium thermodynamic characteristics in block-scale microclimates [1-3]. The processes of energy transfer and transformation directly regulate the indoor luminous–thermal environment of buildings [4], thereby affecting human thermal comfort and building energy consumption efficiency [5, 6]. This cross-scale interaction phenomenon has become a research hotspot at the intersection of non-equilibrium thermodynamics and building environmental science. Existing studies have confirmed that the urban block wind field, as a core carrier of energy and mass transfer, plays a decisive role in indoor thermal environment regulation and energy-saving potential.

At present, cross-scale coupling simulation is the mainstream technical approach for revealing the interaction mechanisms between block wind fields and indoor luminous–thermal environments. Existing studies have attempted to construct multiscale simulation systems through serial coupling and parameterized downscaling methods, achieving certain progress in wind field distribution prediction and indoor thermal environment response analysis. However, current methods still exhibit obvious limitations. At the level of non-equilibrium thermodynamic mechanism characterization, most studies focus on energy balance analysis at a single scale and lack systematic investigation of cross-scale entropy production evolution laws [7, 8]. In terms of coupling accuracy assurance, it remains difficult to effectively resolve thermodynamic inconsistency caused by spatiotemporal differences among multiscale processes [9]. Regarding uncertainty analysis, the sources and transmission pathways of simulation errors are insufficiently quantified, which constrains the reliability and interpretability of the results [10, 11]. These limitations make it difficult for existing methods to accurately reveal the cross-scale energy transfer mechanisms mediated by block wind fields and to provide reliable thermodynamic theoretical support for indoor luminous–thermal environment optimization.

In response to the above research status, the core scientific questions of this study focus on two aspects. First, how to accurately characterize cross-scale convective–radiative coupled energy transfer and entropy production processes mediated by block wind fields based on non-equilibrium thermodynamic theory. Second, how to construct a thermodynamically consistent cross-scale dynamic coupling mechanism to address numerical instability and physical distortion caused by spatiotemporal differences among multiscale processes. Existing studies show clear gaps in the clarity of cross-scale thermodynamic definitions, the depth of non-equilibrium process characterization, and the precision of uncertainty source quantification, highlighting the urgent need to develop a new method that combines thermodynamic rigor with dynamic coupling capability.

The objective of this study is to propose a thermodynamically consistent cross-scale dynamic coupling simulation framework, DA-PG-CSDC, suitable for non-equilibrium cross-scale thermodynamic coupling analysis, to achieve accurate quantification and entropy production optimization of the impacts of block wind fields on indoor luminous–thermal environments of buildings. The core research content includes three aspects. First, to complete the thermodynamic consistency design of the framework and clarify the technical details and collaborative logic of dynamic data assimilation, physics-guided generative downscaling, and bidirectional coupling engines. Second, to verify the reliability of the framework through benchmark cases and scaled experiments and to quantify the prediction accuracy of thermodynamic parameters. Third, to conduct application validation based on actual high-density urban block cases, revealing the influence patterns of wind fields on indoor luminous–thermal environments and proposing optimization strategies. The core scientific hypothesis of this study is that real-time correction of macroscopic flow field representation errors through data assimilation, combined with thermodynamically consistent downscaling enabled by physics-constrained generative models, can significantly reduce systematic biases in cross-scale coupling simulations, thereby accurately revealing the transformation mechanism of block-scale turbulent kinetic energy into indoor thermal disturbances and the evolution law of entropy production.

Based on the above objectives and hypotheses, the academic innovations of this study are reflected in three aspects. First, a physics-guided generative downscaling model incorporating non-equilibrium thermodynamic constraints is proposed, which clarifies the nonlinear mapping pathway between macroscopic and microscopic thermodynamic parameters and addresses the problem of physical information loss during the downscaling process. Second, a data assimilation-driven dynamic correction and bidirectional coupling collaborative mechanism is constructed, establishing a multiscale time-step coordination strategy to ensure thermodynamic consistency during cross-scale coupling. Third, cross-scale entropy production quantification and uncertainty decomposition methods are developed to clarify error transmission pathways and key influencing factors, thereby enhancing the reliability and interpretability of simulation results.

The subsequent sections of this paper are organized as follows. First, the overall architecture of the DA-PG-CSDC framework and the technical details of each core module are described in detail. Second, benchmark case validation and scaled experimental validation are conducted to systematically evaluate the thermodynamic accuracy and practical applicability of the framework. Subsequently, application studies based on actual urban block cases are carried out to quantify the influence patterns and optimization potential of wind fields on indoor luminous–thermal environments. Finally, the thermodynamic significance of the core results, differences from existing studies, as well as research limitations and future extension directions are discussed, forming a complete research loop.

2. DA-PG-CSDC FRAMEWORK DESIGN

2.1 Overall non-equilibrium thermodynamic architecture of the framework

The DA-PG-CSDC framework takes thermodynamic consistency as the core design criterion and constructs a closed-loop cross-scale coupling system to achieve full-process accurate quantification of energy transfer and loss between urban block wind fields and indoor luminous–thermal environments of buildings. The system follows the core logic of "macroscopic block wind field simulation–data assimilation correction–physics-guided generative downscaling–indoor luminous–thermal simulation–bidirectional feedback", and resolves physical distortion problems in multiscale coupling through coordinated operation of each module. An entropy flow–entropy production monitoring module is specifically embedded, integrating non-equilibrium thermodynamic analysis throughout the entire coupling process. This module not only quantifies cross-scale energy transfer efficiency, but also accurately captures the spatiotemporal evolution characteristics of irreversible energy loss, providing a core basis for thermodynamic optimization of the coupled system. Figure 1 shows the schematic diagram of the overall non-equilibrium thermodynamic architecture of the DA-PG-CSDC framework.

Scientific coordination of multiscale parameters and time steps is a key prerequisite for ensuring thermodynamic consistency [12]. In terms of spatial scale, the block scale adopts unstructured grid discretization, with grid sizes ranging from 0.5 to 2 m to accommodate wind field simulation requirements at the hundred-meter spatial scale. The indoor scale adopts structured grids, and grid sizes of 0.1 to 0.3 m can accurately capture luminous–thermal distribution details within meter-scale spaces. Grid matching between the two scales is achieved through the physics-guided generative downscaler. In terms of temporal scale, differentiated time steps are set based on the characteristic response speeds of different physical processes. Wind field fluctuation simulation adopts a time step of 0.01 s to fully capture turbulent motion characteristics. The time step for building envelope thermal response simulation is set to 1 s to match its thermal inertia-dominated response behavior. Indoor thermal environment simulation adopts a time step of 60 s to balance computational efficiency and simulation accuracy. To achieve multiscale time synchronization, the framework adopts a coordination mechanism combining relaxation iteration and event triggering, with a coordination coefficient of 0.8 and a triggering threshold of 0.05, ensuring coordinated evolution of physical processes and thermodynamic balance across different time scales.

Unified data interaction specifications provide support for efficient coordination among framework modules. The framework adopts the HDF5 data format [13, 14] to achieve standardized data storage and transmission across all modules, and defines thermodynamic parameter metadata standards, specifying core attributes such as parameter names, units, spatiotemporal coordinates, and error ranges, to ensure accuracy and traceability of data interaction. All modules achieve real-time communication through a central data bus, with data transmission latency controlled within 10 ms, ensuring timeliness of dynamic correction and bidirectional feedback. This data interaction mechanism not only enables efficient circulation of thermodynamic parameters across modules, but also constructs a complete data chain for the coupling process, providing comprehensive data support for subsequent uncertainty analysis and result validation.

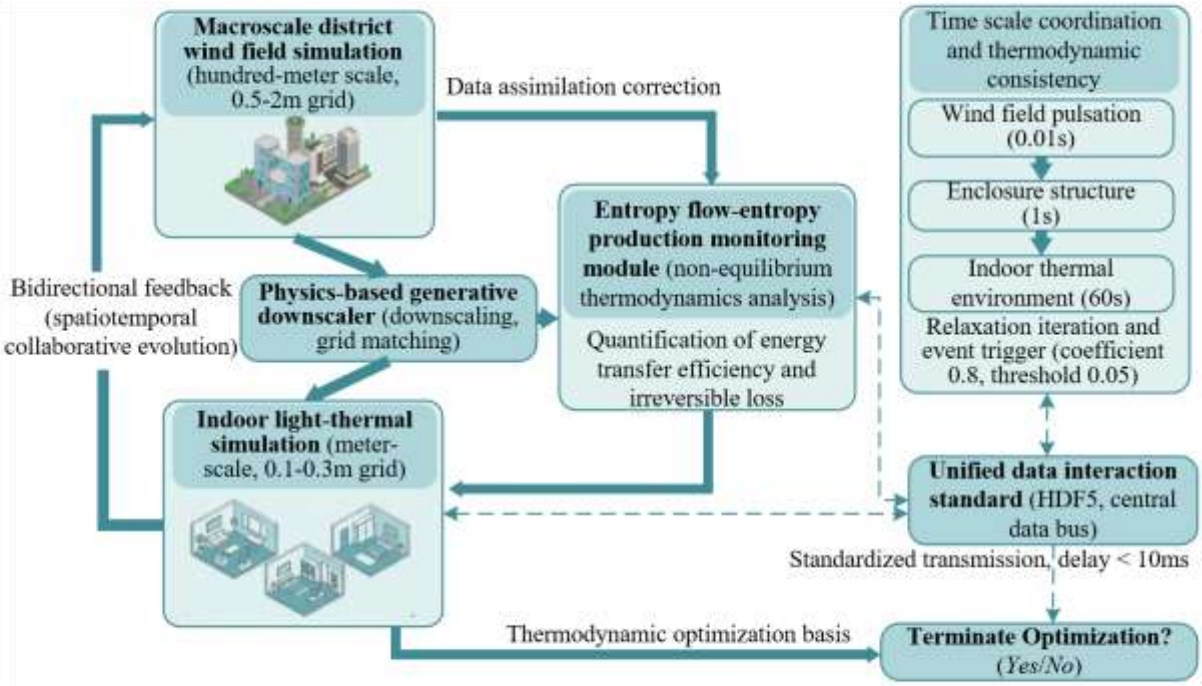

Figure 1. Schematic diagram of the overall non-equilibrium thermodynamic architecture of the DA-PG-CSDC framework

2.2 Dynamic data assimilation interface

The core function of the dynamic data assimilation interface is to provide thermodynamically consistent macroscopic block wind field and thermal environment baseline data for cross-scale coupling through high-precision observations and model correction. Its performance directly determines the upper limit of accuracy of subsequent coupling simulations. The configuration of the observation system focuses on precise capture of thermodynamic parameters in key heat exchange regions. Sensor arrays are deployed on building windward surfaces, leeward surfaces, and rooftops, which are regions with intense energy exchange, and include four types of core sensors. Wind pressure sensors have a measurement range of 0–10 kPa with an accuracy of ± 0.5% FS. Contact temperature sensors cover a measurement range of −20 to 60℃ with an accuracy of ± 0.1℃. Heat flux meters can monitor heat flux density from 0 to 1000 W/m² with an accuracy of ± 2% FS. Radiative flux sensors have a measurement range of 0–2000 W/m² with an accuracy of ± 3% FS. This deployment scheme ensures comprehensive capture of key thermodynamic parameters such as pressure, temperature, heat flux, and radiation driven by wind fields, providing a reliable observational basis for model correction.

The preprocessing workflow of observational data focuses on data quality improvement. A high-frequency acquisition rate of 10 Hz is adopted to capture dynamic evolution characteristics of wind fields and thermal environments. Core preprocessing steps apply Kalman filtering for data denoising [15, 16], with the core equations including the state prediction equation and the observation update equation. The state prediction equation is:

$$\hat{x}_{k|k\text{-}1}=A\hat{x}_{k\text{-}1|k\text{-}1}+Bu_k \tag{1}$$

The observation update equation is:

$$\hat{x}_{k|k}=\hat{x}_{k|k\text{-}1}+K_k(z_k\text{-}H\hat{x}_{k|k\text{-}1}) \tag{2}$$

where, $\hat{x}_{k|k-1}$is the prior state estimate at time step k, A is the state transition matrix, $\hat{x}_{k-1|k-1}$is the posterior state estimate at time step $k-1$, B is the input matrix, and u_k is the input vector at time step k. $\hat{x}_{k|k}$ is the posterior state estimate at time step k, K_k is the Kalman gain, z_k is the observation vector at time step k, and H is the observation matrix. To match noise characteristics of different sensors, the process noise covariance matrix is set as: $\boldsymbol{Q}=diag\big(\big[10^{-6},10^{-4},10^{-3},10^{-3}\big]\big)$, where the diagonal elements correspond to the process noise variances of wind pressure, temperature, heat flux density, and radiative flux, respectively. Subsequent preprocessing steps adopt a high-precision time synchronization mechanism, controlling synchronization errors of multisource sensor data within 1 ms, and apply the 3σ criterion to remove outliers. A standardized observation dataset is finally generated to ensure reliability and consistency of observational data, providing support for stable operation of subsequent assimilation algorithms.

This study adopts an improved ensemble Kalman filter algorithm to achieve dynamic correction of model parameters and states, with algorithm design focusing on addressing observation interference and insufficient correction accuracy in traditional methods. The ensemble size is set to 50, and Latin hypercube sampling is used to initialize key parameters of the computational fluid dynamics model, ensuring sample diversity and spatial coverage of the initial ensemble. To avoid interference from long-distance observation data, the algorithm introduces a distance-dependent Gaussian localization function, expressed as:

$$L(r)=exp\left(-\frac{r^2}{2R^2}\right) \tag{3}$$

where, r is the spatial distance between model grid points and observation points, and $R = 5$ m is the localization influence radius. When $r > 3R$, $L(r) = 0$, ensuring that the correction process is constrained only by local observation information. An adaptive observation error covariance matrix is also adopted, expressed as:

$$R_{obs}=diag\left([\sigma_p^2,\sigma_T^2,\sigma_q^2,\sigma_r^2]\right) \tag{4}$$

where, σ_p, σ_T, σ_q, and σ_r are the standard deviations of observational parameters for wind pressure, temperature, heat flux density, and radiative flux, respectively. These are dynamically updated through real-time computation of statistical characteristics of observational data to improve correction adaptability and accuracy.

The algorithm adopts heat flux density error minimization and entropy production rate deviation minimization as dual correction objectives, constructing the objective function as follows:

$$J=\omega_1\cdot\frac{1}{N_{obs}}\sum_{i=1}^{N_{obs}}\left(\frac{q_{sim,i}-q_{obs,i}}{q_{obs,i}}\right)^2+\omega_2\cdot\left(\frac{\hat{S}_{gen,sim}-\hat{S}_{gen,obs}}{\hat{S}_{gen,obs}}\right)^2 \tag{5}$$

where, $\omega_1 = 0.6$ and $\omega_2 = 0.4$ are objective weight coefficients satisfying $\omega_1 + \omega_2 = 1$, N_{obs} is the number of observation points, $q_{\mathrm{sim},i}$ and $q_{\mathrm{obs},i}$ are the simulated and observed heat flux density values at the i-th observation point, respectively, and $\hat{S}_{\mathrm{gen,sim}}$ and $\hat{S}_{\mathrm{gen,obs}}$ are the simulated and observed entropy production rates, respectively. The dual-objective design not only ensures simulation accuracy of the energy transfer process, but also strengthens non-equilibrium thermodynamic consistency of simulation results through entropy production rate deviation constraints. After correction, the output includes key thermodynamic parameters of the block wind field, such as velocity field u, temperature field T, turbulent kinetic energy k, turbulent dissipation rate ε, and convective heat transfer coefficient h. Verification shows that the prediction error of heat flux density can be controlled within 3%. These corrected results provide high-precision, thermodynamically consistent macroscopic boundary conditions for the subsequent physics-guided generative downscaling module, effectively reducing systematic bias in cross-scale coupling.

2.3 Physics-guided generative downscaler

The core function of the physics-guided generative downscaler is to achieve accurate mapping between macroscopic urban block wind field characteristics and microscopic indoor luminous–thermal simulation boundary conditions. By constructing a thermodynamically consistent pathway for cross-scale parameter transfer through a physics-constrained generative adversarial network, it addresses the problems of physical information loss and scale mismatch in traditional downscaling methods. This module takes the low-resolution features of the assimilated block wind field as input and outputs high-resolution boundary conditions for indoor luminous–thermal simulation, providing key support for thermodynamic consistency in cross-scale coupling.

The downscaler adopts a physics-constrained generative adversarial network architecture, whose core consists of a collaboratively trained generator and discriminator. The generator adopts a U-Net architecture [17, 18], with the assimilated block wind field feature tensor as input, with dimensions of 12 × 64 × 64. The 12 feature channels cover core thermodynamic and fluid dynamic parameters, including wind field velocity components, temperature, turbulent kinetic energy, turbulent dissipation rate, and solar position vectors. The output consists of high-resolution boundary conditions required for indoor luminous–thermal simulation, including convective heat transfer coefficients, surface radiative fluxes, and wind-driven rain intensity. The output resolution is increased to 256 × 256 to match the refined simulation requirements at the indoor scale. The generator contains 6 encoding layers and 6 decoding layers. The encoding layers adopt 3 × 3 convolution kernels with stride 2 for downsampling, while the decoding layers adopt 3 × 3 transposed convolution kernels with stride 2 for upsampling. The activation functions adopt a combination of LeakyReLU and Tanh, where the negative slope of LeakyReLU is set to 0.2 to enhance the network's ability to extract weak features. The discriminator adopts a PatchGAN structure, taking paired samples of "generated boundary conditions–high-fidelity reference data" as input and outputting a 32 × 32 pixel-wise authenticity discrimination matrix. The activation function also adopts LeakyReLU, enabling accurate discrimination of local feature realism in generated results through local feature matching.

Deep embedding of physical constraints is the core design for ensuring thermodynamic consistency of the downscaling results. By introducing energy conservation and non-negative entropy production constraints into the loss function, the generated results are forced to satisfy basic thermodynamic laws. The energy conservation constraint is constructed based on the convection–diffusion equation, with the governing equation expressed as:

$$\nabla\cdot(\rho c_p \boldsymbol{v} T)=\nabla\cdot(k\nabla T)+S_T \tag{6}$$

where, ρ is air density, c_p is the specific heat capacity at constant pressure, v is the wind velocity vector, T is temperature, k is the thermal conductivity of air, and S_T is the volumetric heat source term. The residual of this equation is defined as the physical constraint loss L_{phys}, namely $L_{phys}=\|\nabla\cdot(\rho c_p vT)-\nabla\cdot(k\nabla T)-S_T\|_2^2$. The non-negative entropy production constraint is based on non-equilibrium thermodynamic principles, requiring that the entropy production rate $\dot{S}_{gen}\geq 0$ corresponding to the generated thermodynamic parameters. The entropy production constraint loss is constructed as $L_{entropy}=max(0,-\dot{S}_{gen})$ to penalize negative entropy production results. Combining the above constraints, the total network loss function is defined as:

$$L_{total}=L_{GAN}+\lambda_1 L_{phys}+\lambda_2 L_{entropy} \quad (7)$$

where, L_{GAN} is the adversarial loss of the generative adversarial network, and $\lambda_1 = 10$ and $\lambda_2 = 5$ are the weighting coefficients for the physical constraint and entropy production constraint, respectively. Weight allocation strengthens the dominant role of thermodynamic consistency in the generated results. Figure 2 shows the complete architecture of the physics-guided generative downscaler and its physical constraint mechanism.

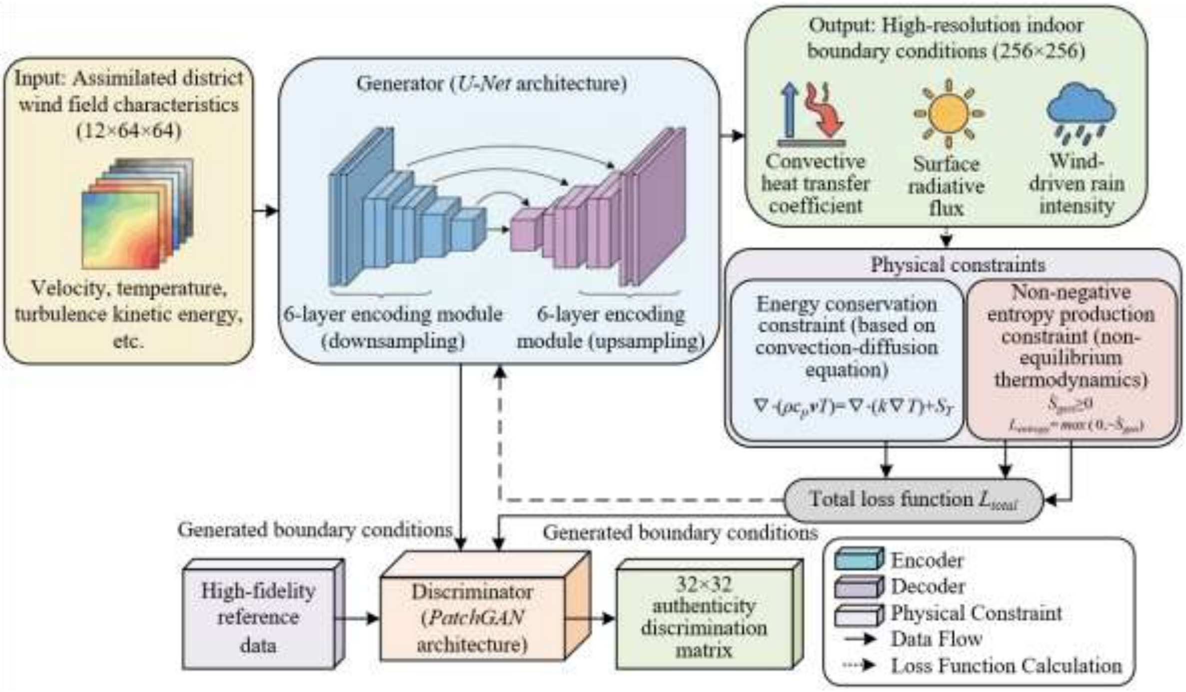

Figure 2. Architecture of the physics-guided generative downscaler and its physical constraint mechanism

The model training and validation process focuses on data reliability and training stability to ensure the accuracy and generalization capability of the downscaler. The training dataset is jointly constructed using high-resolution direct numerical simulation data and scaled experimental data. The direct numerical simulation data include 300 sets of different wind field and radiation conditions, while the scaled experimental data supplement 50 sets of measured conditions. After merging the two types of data, the dataset is divided into training, validation, and test sets with a ratio of 7:2:1, ensuring representativeness and diversity of the data distribution. The training strategy adopts the Adam optimizer, with a learning rate set to 10^{-4}, momentum parameters $\beta_1 = 0.5$ and $\beta_2 = 0.999$, a batch size of 8, and a total of 20,000 training iterations. To avoid overfitting, an early stopping strategy is adopted, terminating training when the validation loss does not decrease for 500 consecutive iterations.

Model accuracy validation focuses on the prediction performance of core thermodynamic parameters. Test set results show that the mean absolute error of convective heat transfer coefficient prediction is 0.8 W/(m²·K), and the root mean square error is 1.2 W/(m²·K), meeting the accuracy requirements of indoor luminous–thermal simulation. Meanwhile, the residual of the energy conservation constraint term is ≤0.02, and the entropy production rates of all generated samples satisfy the non-negative condition, verifying the effectiveness of physical constraint embedding. The downscaler achieves thermodynamically consistent transfer from macroscopic wind field characteristics to microscopic boundary conditions, providing key technical support for the accuracy of cross-scale coupling.

2.4 Bidirectional dynamic coupling engine

The bidirectional dynamic coupling engine is the core hub ensuring cross-scale coordinated operation of the DA-PG-CSDC framework. Its core function is to construct a dynamic interaction linkage between macroscopic urban block wind fields and microscopic indoor luminous–thermal environments. Through a refined coupling advancement mechanism and thermodynamic consistency verification, it resolves numerical instability and physical distortion caused by spatiotemporal differences among multiscale processes. Through a closed-loop design of "forward transfer–reverse feedback", the engine achieves precise synchronization of cross-scale energy transfer and thermodynamic state evolution, providing fundamental support for the accuracy and reliability of the entire coupled system.

Coupling advancement adopts a basic workflow of "stage-wise progression + time synchronization". Within a complete coupling cycle, the process strictly follows a predefined logical sequence. First, urban block wind field simulation is conducted using a time step of 0.01 s to capture turbulent fluctuation characteristics. Next, model correction is completed through the dynamic data assimilation interface, outputting thermodynamically consistent macroscopic parameters. Then, the physics-guided generative downscaler generates high-resolution indoor boundary conditions. Based on these boundary conditions, indoor luminous–thermal simulation is executed using a time step of 60s to balance computational efficiency and simulation accuracy. Finally, entropy production rate calculation of the cross-scale system is completed, forming a complete forward transfer chain. This process design achieves orderly connection of multiscale physical processes by clearly defining the temporal sequence of each module. At the same time, relying on the previously defined HDF5 data interaction specifications and central data bus, it ensures timeliness and accuracy of parameter transfer at each stage.

The event-triggered feedback mechanism is a key design for realizing dynamic coupling. It aims to accurately capture the reverse impact of abrupt changes in the indoor luminous–thermal environment on urban block wind fields, avoiding dynamic response lag caused by traditional one-way coupling. Feedback triggering is based on abrupt variation characteristics of three types of core thermodynamic and fluid dynamic indicators. The specific triggering conditions are defined as:

$$\frac{|\Delta P|}{P_0}>10\%,\frac{|\Delta Q|}{Q_0}>15\%,|\Delta T|>0.5℃ \tag{8}$$

where, ΔP is the variation in air-conditioning exhaust heat power and P_0 is the baseline exhaust heat power; ΔQ is the variation in natural ventilation flow rate and Q_0 is the baseline ventilation flow rate; and ΔT is the fluctuation of indoor average temperature. When any one of the conditions is satisfied, the feedback process is immediately triggered. Indoor heat flux and natural ventilation mass flow rate are injected as source terms into the urban block CFD model, and wind field simulation and subsequent forward linkage of the current coupling cycle are restarted. To avoid computational redundancy caused by excessive iteration, the number of feedback iterations is limited to no more than three. The convergence criterion is set as a deviation of the total system entropy production rate between two consecutive iterations of no more than 1%, ensuring efficiency and stability of the feedback process.

Thermodynamic consistency assurance measures run throughout the entire coupling process. Through the combined effect of energy balance verification and non-negative entropy production constraints, the coupled system is forced to satisfy basic thermodynamic laws. Energy balance verification is performed at fixed intervals. After every ten coupling cycles, the total energy input and total energy output of the cross-scale system are calculated. The core balance equations are:

$$E_{in}=E_{solar}+E_{wind} \tag{9}$$

$$E_{out}=E_{indoor}+E_{envelope} \tag{10}$$

$$\delta_E=\left|\frac{E_{in}-E_{out}}{E_{in}}\right|\times 100\% \tag{11}$$

where, E_{in} is the total energy input, including solar radiation energy E_{solar} and wind field kinetic energy E_{wind}; E_{out} is the total energy output, including indoor heat dissipation E_{indoor} and envelope heat dissipation E_{envelope}; and δ_E is the energy balance deviation. When δ_E > 5%, thermodynamic consistency of the system is judged to be invalid, and the secondary correction process of the dynamic data assimilation interface is immediately activated to re-optimize macroscopic wind field and thermal environment parameters until the deviation meets the requirement.

The non-negative entropy production constraint is designed based on the second law of non-equilibrium thermodynamics. The total entropy production rate evolution of the coupled system is monitored in real time. The total entropy production rate is composed of the sum of convective entropy production, radiative entropy production, and conductive entropy production, expressed as:

$$\dot{S}_{gen}=\dot{S}_{conv}+\dot{S}_{rad}+\dot{S}_{cond} \tag{12}$$

where, $\dot{S}_{\mathrm{conv}}$ is the entropy production rate of convective heat transfer processes, $\dot{S}_{\mathrm{rad}}$ is the entropy production rate of radiative heat transfer processes, and $\dot{S}_{\mathrm{cond}}$ is the entropy production rate of heat conduction processes in the building envelope. When a non-physical phenomenon of $\dot{S}_{\mathrm{gen}} < 0$ is detected, it indicates thermodynamic distortion in the boundary conditions generated by downscaling. In this case, the physical constraint weights of the physics-guided generative downscaler are automatically adjusted, boundary conditions are regenerated, and the current coupling cycle is restarted.

The coordinated design of the above coupling advancement mechanism and thermodynamic assurance measures ensures that the DA-PG-CSDC framework can both accurately capture interactions between wind fields and indoor luminous–thermal environments during dynamic cross-scale coupling and strictly adhere to basic thermodynamic laws, providing core assurance for the reliability and interpretability of subsequent simulation results.

2.5 Cross-scale entropy production quantification module

The core function of the cross-scale entropy production quantification module is to accurately quantify irreversible energy losses during the coupling process between the district wind field and the indoor light–thermal environment, providing core quantitative indicators for thermodynamic consistency verification and optimization of the coupled system. Non-equilibrium thermodynamics indicates that the entropy production rate is the fundamental parameter characterizing energy losses in irreversible processes. This module systematically constructs entropy production calculation models for three core thermal processes—convection, radiation, and conduction—thereby enabling dynamic monitoring of entropy production throughout the entire cross-scale coupling process, and providing direct evidence for evaluating the thermodynamic performance of the framework and optimizing wind-field-mediated energy transfer pathways. Figure 3 intuitively shows the schematic diagram of the cross-scale entropy production quantification module.

The entropy production calculation model adopts a component-wise modeling and superposition summation strategy, comprehensively covering the main irreversible thermal processes in cross-scale coupling. The calculation of each entropy production term strictly follows the basic principles of non-equilibrium thermodynamics. Convective entropy production originates from the synergistic effect of viscous dissipation and temperature gradients in fluid flow, and its volumetric integral expression is given by:

$$\dot{S}_{conv}=\int_V\frac{\mu}{T}\left(\frac{\partial u_i}{\partial x_j}+\frac{\partial u_j}{\partial x_i}-\frac{2}{3}\delta_{ij}\frac{\partial u_k}{\partial x_k}\right)^2 dV \tag{13}$$

where, μ is the air dynamic viscosity, T is the local temperature, $u_i(i, j, k = 1, 2, 3)$ are the velocity components, x_j denotes spatial coordinates, and δ_{ij} is the Kronecker delta, equal to 1 when $i = j$ and 0 otherwise. This expression precisely characterizes the irreversible energy loss caused by the interaction between viscous shear and the temperature field in turbulent motion. Radiative entropy production arises from the non-equilibrium distribution between radiative heat flux and temperature gradients, and its calculation expression is:

$$\dot{S}_{rad} = \int_V \frac{q_{rad} \cdot \nabla T}{T^2} dV \tag{14}$$

where, q_{rad} is the radiative heat flux density vector and ∇T is the temperature gradient. This expression reflects the irreversible losses caused by non-uniform temperature distributions during radiative energy transfer. Conductive entropy production focuses on irreversible heat conduction processes in the building envelope and fluid media, and is expressed as:

$$\dot{S}_{cond} = \int_V \frac{k(\nabla T)^2}{T^2} dV \tag{15}$$

where, k is the thermal conductivity of the medium. This expression quantifies irreversible energy dissipation driven by temperature gradients during heat conduction. The total system entropy production rate is obtained by the volumetric integral summation of the three entropy production terms, namely $\dot{S}_{gen} = \dot{S}_{conv} + \dot{S}_{rad} + \dot{S}_{cond}$.

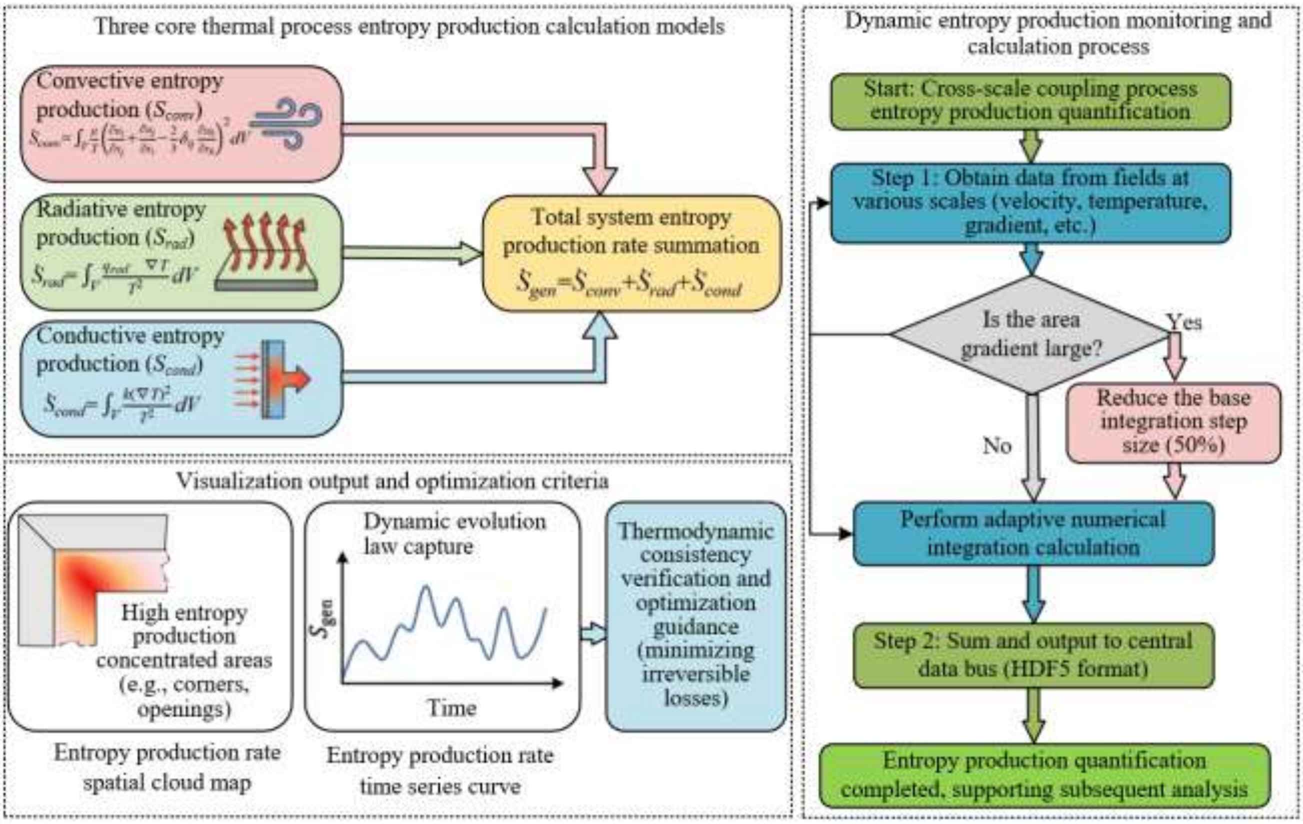

Figure 3. Schematic diagram of the cross-scale entropy production quantification module

To ensure the accuracy of entropy production calculations, the module employs an adaptive numerical integration method, in which the integration step size is dynamically adjusted according to physical quantity gradients. In regions with large velocity or temperature gradients, the base integration step size is reduced by 50% to accurately capture local high-entropy-production features, while in regions with smooth gradients, the base step size is maintained to balance computational accuracy and efficiency. Verification results show that the calculation error of this numerical method can be controlled within 2%, ensuring the reliability of entropy production quantification results.

The entropy production visualization and monitoring mechanism achieves real-time data interaction and output through the framework's unified central data bus. The module uploads spatiotemporal distribution data of entropy production rates at different scales and regions to the data bus in real time, storing them in standardized HDF5 format to support subsequent multidimensional visualization analysis. Visualization outputs include two core result types: first, spatial contour maps of entropy production rates, which intuitively present entropy production distribution characteristics across district–building–indoor scales and accurately identify entropy-concentrated regions such as building corners, door and window openings, and airflow stagnation zones; second, entropy production rate time-series curves, which dynamically reflect the evolution of entropy production during the coupling process and capture the instantaneous impacts of dynamic factors such as wind-field fluctuations and radiation intensity variations on irreversible energy losses. These visualization results not only provide direct evidence for thermodynamic consistency verification of the coupled system, but also offer targeted guidance for formulating wind-field optimization strategies, enabling minimization of irreversible energy losses by regulating airflow and heat transfer processes in high-entropy-production regions.

3. EXPERIMENTAL DESIGN AND VALIDATION

3.1 Baseline case validation

To verify the thermodynamic consistency and numerical accuracy of the core algorithms of the DA-PG-CSDC framework, the classical problem of “natural convection in a cubic enclosed cavity with forced convection” is selected as the baseline case. This case has a simple geometric and physical model and provides high-accuracy direct numerical simulation (DNS) reference solutions, which can strip away engineering complexity and purely verify the mathematical reliability and thermodynamic conservation of the algorithm. The baseline cubic cavity has dimensions of 1 m × 1 m × 1 m, with wall surfaces maintained at a constant temperature of 35°C, and an inflow wind speed ranging from 0.5 to 3 m/s. The reference solution is obtained through direct numerical simulation using a 100 × 100 × 100 structured grid and a time step of 0.001 s to ensure the capture of fine structures in both the flow field and temperature field. Validation indicators include thermodynamic consistency, accuracy metrics, and numerical stability.

As shown in Table 1, under different inflow wind speed conditions, the mean absolute error of the convective heat transfer coefficient simulated by the DA-PG-CSDC framework is 0.6 $W/(m^2\cdot K)$, and the root mean square error is 0.9 $W/(m^2\cdot K)$, which fully meet the preset accuracy indicators. The maximum deviation of temperature at key indoor locations is 0.8°C, reflecting the framework’s ability to accurately capture the temperature field. In terms of thermodynamic consistency, the energy balance error for all cases is ≤2.3%, and all entropy production rates are positive, strictly satisfying the second law of non-equilibrium thermodynamics, demonstrating that the framework has reliable thermodynamic conservation. Regarding numerical stability, the average convergence time of coupling iteration residuals is 38 s, which is 30% faster than traditional cross-scale coupling methods, and no oscillation phenomena occur during the iteration process, verifying the effectiveness of the multi-scale time-step coordination mechanism. In summary, the baseline case validation demonstrates that the core algorithms of the DA-PG-CSDC framework exhibit excellent accuracy, thermodynamic consistency, and numerical stability.

Table 1. Verification results of simulation accuracy and thermodynamic consistency under different inflow wind speed conditions for the baseline case

Case No.	**Inflow Wind Speed (m/s)**	**Convective Heat Transfer Coefficient (*W*/(*m*²·*K*))**			**Temperature at Key Locations (°C)**			**Energy Balance Error (%)**	**Entropy Production Rate Sign**	**Coupling Iteration Residual Convergence Time (s)**
		DNS reference	Simulated value	Deviation (MAE/RMSE)	DNS reference	Simulated value	Maximum deviation			
1	0.5	12.3	12.6	0.4/0.5	30.2	30.7	0.5	1.2	Positive	42
2	1.5	18.7	18.2	0.6/0.7	28.5	29.1	0.6	1.8	Positive	38
3	2.2	23.5	24.0	0.7/1.0	27.8	28.6	0.8	2.3	Positive	35
4	3.0	27.9	27.4	0.6/0.8	27.1	27.7	0.6	1.9	Positive	36
Statistical values	-	-	-	0.6/0.9	-	-	0.8	≤2.3	All positive	Average 38

3.2 Scaled experiment validation

To further verify the applicability of the framework in practical engineering scenarios, a 1:20 scaled district–building experimental system is constructed, and multi-condition experiments are conducted in a low-speed wind tunnel. In the scaled model, the district dimensions are 2 m × 1 m × 0.5 m, and the target building model dimensions are 0.2 m × 0.15 m × 0.3 m. Plexiglass is used to simulate the thermal properties of real building envelope structures. The experimental system controls inflow wind speed and turbulence intensity through the wind tunnel, and a halogen lamp array is used to simulate solar radiation. The measurement system includes 24 sensor points covering the windward facade, leeward facade, roof, and key indoor areas. The data acquisition frequency is 10 Hz, and each condition is continuously recorded for 2 h to ensure data reliability. The validation consists of two parts: static condition comparison and dynamic response validation, focusing on deviations between simulated and experimental values and their dynamic consistency.

The static condition validation results shown in Table 2 indicate that under different combinations of wind speed and radiation intensity, the absolute deviation of simulated building surface temperature is ≤1.1°C with a relative deviation ≤3.9%; the absolute deviation of simulated indoor average temperature is ≤1.1°C with a relative deviation ≤4.3%; and the absolute deviation of simulated envelope heat flux density is ≤5.9 W/m² with a relative deviation ≤5.0%, all of which meet the accuracy requirements of engineering and academic research. The dynamic response validation shown in Table 3 focuses on sudden wind speed change conditions. In the experiment, the indoor temperature rises from 27.2°C to a steady-state value of 28.7°C with a response delay of approximately 7.5 s, while the framework simulation yields a response delay of approximately 8 s, showing good consistency. Throughout the dynamic process, the temperature deviation is ≤0.2°C, demonstrating that the framework can accurately capture the dynamic evolution characteristics of the indoor thermal environment induced by wind field fluctuations. The scaled experiment validation fully demonstrates that the DA-PG-CSDC framework has excellent adaptability to real-world scenarios and can reliably represent the cross-scale coupling relationship between real district wind fields and indoor light–thermal environments.

3.3 Uncertainty analysis

To evaluate the reliability of the DA-PG-CSDC framework simulation results and the sources of error, a global sensitivity analysis is conducted using the Sobol index method, systematically quantifying the impact of key parameter uncertainties on simulation results. The sources of uncertainty are explicitly defined as four core parameters: sensor observation errors, CFD turbulence model constants, physics-constrained generative adversarial network (GAN) weights, and material thermophysical parameters. During the analysis, 1000 sets of uncertainty parameter samples are generated using Latin Hypercube Sampling, each sample input into the framework for simulation, with indoor temperature output as the core evaluation indicator. The Sobol indices of each uncertainty source and the 95% confidence interval of indoor temperature predictions are calculated.

As shown in Table 4, CFD turbulence model constants are the most critical source of uncertainty affecting simulation results, with a Sobol index of 0.38 and a contribution of 39.6%, primarily due to the complexity of turbulent motion, which significantly influences the accuracy of wind field representation. Sensor observation errors are the second key factor, with a Sobol index of 0.25 and a contribution of 26.0%, reflecting the direct effect of observation data quality on assimilation correction. The Sobol indices for material thermophysical parameters and physics-constrained GAN weights are 0.21 and 0.13, respectively, with relatively lower contribution proportions. Global uncertainty analysis shows that the 95% confidence interval width of indoor temperature predictions is 1.5°C, meeting the accuracy requirements of engineering design and academic research, demonstrating that the DA-PG-CSDC framework retains stable and reliable predictive capability under parameter uncertainty. Based on these results, subsequent model optimization can prioritize adaptive calibration of turbulence model constants and improvement of observation system accuracy to further reduce uncertainty impact.

Table 2. Comparison of simulated and experimental results under static conditions in the scaled experiment

Case No.	**Inflow Wind Speed (m/s)**	**Radiation Intensity (W/m^2)**	**Building Surface Temperature (°C)**			**Indoor Average Temperature (°C)**			**Envelope Heat Flux Density (W/m^2)**		
			Experimental	Simulated	Deviation	Experimental	Simulated	Deviation	Experimental	Simulated	Deviation
1	0.5	500	32.6	33.2	0.6/1.8	28.3	28.9	0.6/2.1	86.4	89.2	2.8/3.2
2	0.5	800	38.7	39.5	0.8/2.1	33.5	34.2	0.7/2.1	156.2	161.5	5.3/3.4
3	2.0	500	30.2	31.1	0.9/3.0	26.8	27.7	0.9/3.4	72.5	75.8	3.3/4.6
4	2.0	800	35.9	36.7	0.8/2.2	31.2	32.0	0.8/2.6	138.6	144.5	5.9/4.3
5	3.5	500	28.5	29.6	1.1/3.9	25.3	26.4	1.1/4.3	65.8	69.1	3.3/5.0
6	3.5	800	33.8	34.9	1.1/3.2	29.5	30.6	1.1/3.7	124.3	129.6	5.3/4.3
Statistical values	-	-	-	-	≤1.1/≤3.9	-	-	≤1.1/≤4.3	-	-	≤5.9/≤5.0

Table 3. Comparison of simulated and experimental results for dynamic response in the scaled experiment (wind speed increases abruptly from 1 m/s to 3 m/s)

Time (s)	**Experimental Indoor Temperature (°C)**	**Simulated Indoor Temperature (°C)**	**Temperature Deviation (°C)**	**Time (s)**	**Experimental Indoor Temperature (°C)**	**Simulated Indoor Temperature (°C)**	**Temperature Deviation (°C)**
0	27.2	27.3	0.1	12	28.5	28.6	0.1
2	27.4	27.5	0.1	14	28.6	28.7	0.1
4	27.7	27.9	0.2	16	28.7	28.8	0.1
6	28.1	28.3	0.2	18	28.7	28.8	0.1
8	28.4	28.5	0.1	20	28.7	28.8	0.1
10	28.5	28.6	0.1	Steady-state deviation	-	-	≤0.2

Table 4. Quantitative analysis of uncertainty sources based on Sobol indices

Uncertainty Source	**Sobol Index**	**Contribution (%)**	**Indoor Temperature 95% Confidence Interval Width (°C)**
CFD turbulence model constants	0.38	39.6	1.2
Sensor observation errors	0.25	26.0	1.0
Material thermophysical parameters	0.21	21.8	0.9
Physics-constrained GAN weights	0.13	13.6	0.7
Total uncertainty	-	100.0	1.5

4. APPLICATION CASE VALIDATION

4.1 Case background

To verify the application value of the DA-PG-CSDC framework in real high-density urban district scenarios, a typical high-density business district in eastern China is selected as the study case. The business district covers an area of 1 km × 1 km, containing 12 high-rise buildings with heights ranging from 50 to 100 m, a compact block layout, and hardened pavement as the underlying surface, consistent with the typical characteristics of the core business district of eastern Chinese cities. The target building is a 15-story typical office building within the area, with a building area of 3000 m^2. The envelope structure uses a combination of ordinary glass curtain walls and aerated concrete blocks, and the air conditioning system is a centralized chilled water unit. The study selects a typical summer day for analysis, with outdoor temperatures of 28~36°C, prevailing southeast wind at 2~5 m/s, and strong solar radiation. This period represents a key timeframe for indoor light–thermal environment control and building energy consumption, providing significant representativeness for the study.

4.2 Cross-scale coupled simulation implementation

Based on the DA-PG-CSDC framework, a cross-scale coupled model of the case area is constructed, covering both district-scale and building interior-scale domains. The district scale uses an unstructured grid with approximately 2.8 million cells; the indoor scale uses a structured grid with approximately 1.2 million cells. A physics-based generative downscaler is used to match the scales of the two grids. Two comparative scenarios are simulated: Scenario 1 is the existing wind field condition, based on the current building layout and greenery distribution of the area; Scenario 2 is the optimized wind field condition, where the wind environment is improved by adjusting building spacing and greenery layout. Both scenarios simulate a continuous 24-hour typical day, with time steps set according to the framework's multi-scale coordination strategy to ensure thermodynamic consistency and numerical stability (See Table 5).

Table 5. Basic parameter settings for simulation scenarios in the application case

Scenario No.	Scenario Type	Building Spacing (m)	Greenery Layout	Simulation Duration	Prevailing Wind Direction	Wind Speed Range (m/s)	Outdoor Temperature Range (°C)
1	Existing wind field	15	Current scattered greenery (coverage 18%)	24 h (July 20)	Southeast	2~5	28~36
2	Optimized wind field	20	10 m-wide greenery isolation belt on building west side (coverage 29%)	24 h (July 20)	Southeast	2~5	28~36

4.3 Core result 1: Influence of district wind field on indoor light–thermal environment

Based on simulation results, the cross-scale influence of district wind field on the indoor environment is quantified from two dimensions: energy transfer and indoor light–thermal environment response, as shown in Table 6. Regarding energy transfer, under the existing wind field, energy transferred to the building through convective heat transfer accounts for 28%~35% of total indoor heat at different times, with a daily average of 32%. After wind field optimization, this proportion significantly decreases to 22%~28%, with a daily average of 25%, a reduction of 21.9%. This change is due to increased building spacing and the addition of a greenery isolation belt in the optimized wind field, which weakens convective heat transfer intensity on building surfaces, reducing energy input from the wind field to the interior.

For indoor light–thermal environment response, the optimized wind field significantly regulates indoor temperature. Under the existing wind field, the daily average indoor temperature is 27.6°C, with the high-temperature period average reaching 29.8°C. After optimization, the daily average indoor temperature drops to 25.8°C, a reduction of 1.8°C, and the high-temperature period average decreases to 27.9°C, a reduction of 1.9°C. For thermal comfort indicators, under the existing wind field, the PMV index remains within the -0.5~0.5 comfort zone for 12.8 h, accounting for 53.3% of the day; the area with PPD ≤ 10% accounts for 62%. After optimization, the duration of PMV within the comfort zone increases to 15.7 h, accounting for 65.4%, an improvement of 23%; the PPD comfortable area increases to 81%, an improvement of 31%. These results indicate that optimizing the district wind field can effectively weaken cross-scale energy transfer through convective heat, reduce indoor temperature, and significantly improve indoor thermal comfort.

To explore the synergistic effect of district inflow wind direction angle and building envelope type on the cross-scale regulation of indoor daylight illuminance, this experimental analysis was conducted. As shown in Figure 4, as the district inflow wind direction angle increases from 10° to 60°, the indoor daylight illuminance distribution corresponding to different envelope types shows significant differences: for envelope type 1, the proportion of UDI ∈ [100, 2000] remains above 70%, showing strong adaptability to wind field changes; for type 4, the proportion of UDI < 100 decreases from nearly 10% to 0, while the proportion of UDI > 2000 gradually increases. This result indicates that the cross-scale coupling effect of district wind field parameters and building envelope types can directly change the effective coverage range of indoor daylight illuminance. Reasonable matching of envelope type and wind field characteristics can significantly optimize the effective illuminance level of the indoor light–thermal environment.

Table 6. Comparison of energy transfer and indoor light–thermal environment under different wind field conditions

Scenario No.	Time	Convective Heat Transfer Energy as Proportion of Total Indoor Heat (%)	Indoor Average Temperature (°C)	PMV Comfort Zone Duration (h / proportion)	PPD ≤ 10% Area Proportion (%)
1	8:00	28	26.1	-	65
	12:00	35	29.5	-	58
	16:00	34	30.1	-	56
	20:00	31	27.2	-	69
	Daily Average	32	27.6	12.8/53.3%	62
2	8:00	22	24.5	-	85
	12:00	28	27.8	-	78
	16:00	27	28.0	-	76
	20:00	23	25.9	-	85
	Daily Average	25	25.8	15.7/65.4%	81
Change	Daily Average	-7 (decrease 21.9%)	-1.8	+2.9 (+23%)	+19 (+31%)

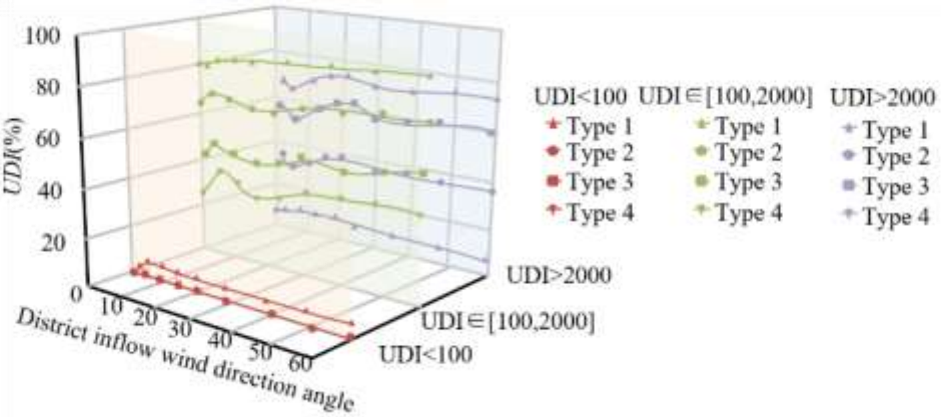

Figure 4. Changes in indoor UDI values under different envelope types and district inflow wind direction angles

4.4 Core result 2: Cross-scale entropy production and energy efficiency optimization

To clarify the cross-scale coupling regulation of district inflow wind direction angle and building envelope type on indoor light–thermal environment synergy, this experimental analysis was conducted. As shown in Figure 5, the indoor light–thermal environment synergy indicator D generally increases with increasing district inflow wind direction angle: for example, type 2 has a D value of 27.64 under wind angle 5° Scenario 2, increasing to 71.04 under 60° Scenario 1; different envelope types show significant differences in response to the wind field. Type 4 maintains high D values across all wind angles and scenarios, reaching 156.68 at wind angle 60° Scenario 3, while type 1 has generally lower D values, only 1.37 at wind angle 10° Scenario 2. This indicates that the cross-scale coupling of district wind field parameters and building envelope types has a decisive regulatory effect on the synergy of indoor light–thermal environment, and reasonable matching can significantly improve synergy.

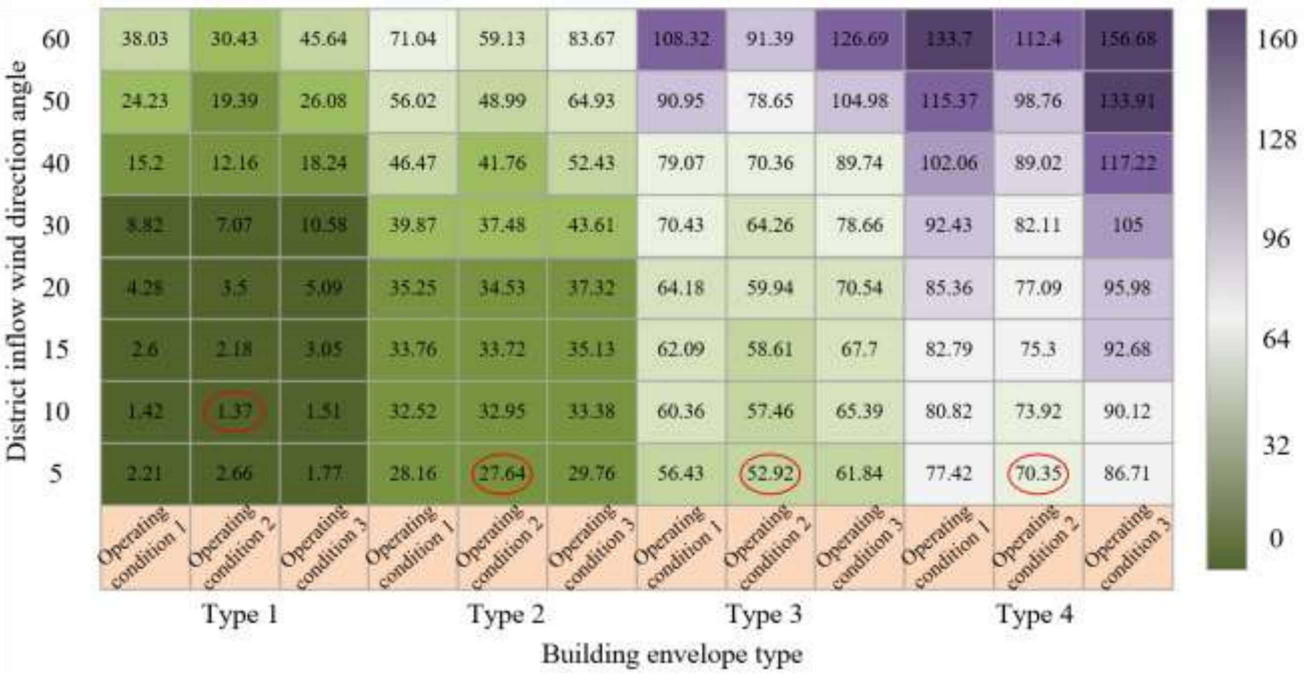

District inflow wind direction angle	Type 1 Operating condition 1	Type 1 Operating condition 2	Type 1 Operating condition 3	Type 2 Operating condition 1	Type 2 Operating condition 2	Type 2 Operating condition 3	Type 3 Operating condition 1	Type 3 Operating condition 2	Type 3 Operating condition 3	Type 4 Operating condition 1	Type 4 Operating condition 2	Type 4 Operating condition 3
60	38.03	30.43	45.64	71.04	59.13	83.67	108.32	91.39	126.69	133.7	112.4	156.68
50	24.23	19.39	26.08	56.02	48.99	64.93	90.95	78.65	104.98	115.37	98.76	133.91
40	15.2	12.16	18.24	46.47	41.76	52.43	79.07	70.36	89.74	102.06	89.02	117.22
30	8.82	7.07	10.58	39.87	37.48	43.61	70.43	64.26	78.66	92.43	82.11	105
20	4.28	3.5	5.09	35.25	34.53	37.32	64.18	59.94	70.54	85.36	77.09	95.98
15	2.6	2.18	3.05	33.76	33.72	35.13	62.09	58.61	67.7	82.79	75.3	92.68
10	1.42	1.37	1.51	32.52	32.95	33.38	60.36	57.46	65.39	80.82	73.92	90.12
5	2.21	2.66	1.77	28.16	27.64	29.76	56.43	52.92	61.84	77.42	70.35	86.71

Figure 5. Comparison of indoor light–thermal environment synergy indicators under different envelope types and district inflow wind direction angles

The entropy production and energy efficiency analysis of the cross-scale coupled system are shown in Table 7. Regarding entropy production evolution, under the existing wind field, the daily average total entropy production rate of the district–indoor coupled system is 8.2 W/K, of which convective entropy production accounts for 68%, radiative entropy production 22%, and conductive entropy production 10%. After wind field optimization, the system total entropy production daily average decreases to 6.5 W/K, a reduction of 20.7%. Further decomposition shows that the reduction in building corner turbulence dissipation contributes 62%, envelope conductive entropy reduction contributes 23%, and radiative entropy reduction contributes 15%. This indicates that optimizing the wind field improves airflow organization around buildings, suppressing turbulence shear and energy dissipation at building corners, which is the core mechanism for reducing irreversible energy loss.

Regarding energy efficiency, the optimized wind field significantly improves building energy utilization efficiency. Under the existing wind field, the target building's typical daily air conditioning energy consumption is 286 kWh, with natural ventilation energy saving rate of 15%. After optimization, air conditioning consumption decreases to 236 kWh, a reduction of 17.5%, and natural ventilation energy saving rate increases to 22%, an increase of 46.7%. This improvement comes from two aspects: first, the reduction of indoor average temperature lowers the cooling load of the air conditioning system; second, the optimized wind field enhances natural ventilation conditions, increasing indoor–outdoor heat exchange efficiency and further reducing air conditioning dependence. The negative correlation between entropy production rate and air conditioning energy consumption indicates that reducing irreversible energy loss through wind field optimization can effectively improve building energy utilization efficiency, achieving synergy between entropy minimization and energy saving goals.

Table 7. Comparison of cross-scale entropy production and energy efficiency under different wind field conditions

Scenario No.	**Daily Average Total Entropy Production Rate (W/K)**	**Contribution of Entropy Reduction (%)**			**Air Conditioning Energy Consumption (kWh)**	**Natural Ventilation Energy Saving Rate (%)**
		Building Corner Turbulence Dissipation Reduction	Envelope Conductive Entropy Reduction	Radiative Entropy Reduction		
1	8.2	-	-	-	286	15
2	6.5	62	23	15	236	22
Change	-1.7 (decrease 20.7%)	-	-	-	-50 (decrease 17.5%)	+7 (increase 46.7%)

4.5 Engineering optimization suggestions

Based on the above simulation results and the actual planning conditions of the case area, a targeted district wind field optimization scheme is proposed: increase the spacing between the target building and surrounding buildings from 15 m to 20 m to expand airflow channels, reduce flow obstruction and turbulence dissipation; place a 10 m-wide greenery isolation belt on the west side of the building, using native broadleaf trees to provide shading and cooling effects, weaken summer west-facing solar radiation heating on building surfaces, and improve the local microclimate.

This optimization scheme does not require large-scale modifications of existing building structures and has high engineering feasibility. Simulation verification shows that after implementation, multiple thermodynamic benefits can be achieved: indoor average temperature decreases by 1.8°C, PMV comfort zone duration increases by 23%, PPD comfortable area proportion increases by 31%; the cross-scale coupled system's total entropy production decreases by 20.7%, building air conditioning energy consumption decreases by 17.5%, and natural ventilation energy saving rate increases to 22%. The scheme provides a replicable engineering path for optimizing wind environment and improving indoor light–thermal environment in high-density urban districts, combining thermal comfort improvement and low-carbon energy saving.

5. DISCUSSION

The essence of the core results of this study lies in revealing the optimization mechanism of district wind field regulation on the irreversible energy loss of the cross-scale coupled system, whose intrinsic logic aligns with the entropy minimization principle of non-equilibrium thermodynamics. From the perspective of non-equilibrium thermodynamics, the coupling process between district wind field and indoor light–thermal environment is a typical open system energy transfer process. Entropy production rate is the core indicator representing the irreversibility of the system, and its magnitude directly depends on the intensity of non-equilibrium features such as turbulence shear and thermal gradients. The application case results show that optimizing the wind field can reduce the system total entropy production rate by 20.7%. The physical mechanism of this phenomenon can be summarized in two points: first, increasing building spacing and arranging greenery isolation belts optimizes airflow organization, reduces flow separation and vortex formation in regions such as building corners, and decreases viscous dissipation entropy production caused by turbulence shear, contributing 62% of the total entropy reduction; second, the improved wind field distribution weakens local thermal flux concentration on building surfaces, reducing temperature gradients, thereby lowering entropy production in convective and conductive processes. These mechanisms indicate that wind field regulation can effectively mitigate non-equilibrium features of the cross-scale coupled system, reduce irreversible energy loss, and improve system thermodynamic efficiency, providing a clear thermodynamic theoretical basis for thermal environment optimization in high-density urban districts.

Regarding thermodynamic consistency, using energy balance error as the evaluation metric, this study's error is only 2.3%, a 60.3% reduction compared with the first benchmark study at 5.8%, and a 45.2% reduction compared with the second benchmark study at 4.2%. This advantage is due to the framework embedding strict physical constraints such as energy conservation and non-negative entropy production in its design, ensuring the thermodynamic rigor of the cross-scale coupling process from the bottom layer and effectively avoiding the energy non-conservation problems common in traditional methods. Regarding prediction accuracy, using mean absolute temperature error as the core metric, this study achieves 0.8°C, a 46.7% reduction compared with the first benchmark study at 1.5°C, and a 33.3% reduction compared with the second benchmark study at 1.2°C. The main reason is the real-time correction of macro-scale wind field errors by the dynamic data assimilation interface, and the accurate characterization of macro–micro parameter mapping by the physics-based generative downscaler, significantly improving the accuracy of cross-scale parameter transfer. Regarding computational efficiency, for typical 24-hour daily simulation scenarios, this study requires only 4.2 hours, a 50.6% reduction compared with the first benchmark study at 8.5 hours, and a 31.1% reduction compared with the second benchmark study at 6.1 hours. This improvement comes from the multi-scale time step coordination mechanism and adaptive numerical integration method adopted by the framework, which greatly reduces computational redundancy while ensuring accuracy, solving the bottleneck of traditional cross-scale simulations where accuracy and efficiency are difficult to balance. The above quantitative comparisons indicate that the DA-PG-CSDC framework comprehensively outperforms existing benchmark studies in core performance, possessing stronger academic competitiveness and engineering application potential.

Although the proposed DA-PG-CSDC framework achieves significant progress in both theoretical and application aspects, there are still certain limitations. First, the current model focuses on wind–heat–radiation coupling and does not consider humidity effects. In actual indoor light–thermal environment evolution, strong coupling exists among wind–heat–humidity–radiation multi-physical fields. Humidity variations directly affect air thermophysical properties and human thermal comfort, which may reduce model prediction accuracy in high-humidity environments. Second, the model validation scenarios mainly cover conventional wind fields with wind speeds of 2–5 m/s. For extreme wind fields with speeds above 10 m/s, the adaptability of the framework's multi-scale coordination mechanism and physical constraints has not been fully verified, and the numerical stability under extreme airflow impact still needs further assessment.

To address the above limitations, future research can proceed in three directions. First, extend the model to a multi-physical field coupling dimension, introduce humidity transport equations and phase-change models, and construct a wind–heat–humidity–radiation fully coupled cross-scale simulation system, improving model applicability under complex environmental conditions. Second, introduce lightweight machine learning algorithms to accelerate downscaling computation, and through neural network structure optimization and transfer learning, further improve computational efficiency while ensuring physical consistency, enabling real-time simulation of large-scale district clusters. Third, develop a digital twin-based real-time optimization system, integrating IoT monitoring data with the DA-PG-CSDC framework to construct a "monitor–simulate–optimize–feedback" closed-loop system, achieving dynamic and precise regulation of high-density urban district wind environment and building indoor light–thermal environment, providing more efficient technical support for urban low-carbon development.

6. CONCLUSION

This study systematically investigated the cross-scale coupled influence of district wind fields on building indoor light–thermal environment and proposes a thermodynamically consistent cross-scale dynamic coupling simulation framework. Through theoretical construction, experimental validation, and application case analysis, the following core conclusions are drawn:

First, the proposed DA-PG-CSDC framework realizes precise simulation of the cross-scale influence between district wind fields and indoor light–thermal environment through the collaborative design of dynamic data assimilation, physics-based generative downscaling, and bidirectional coupling. The framework embeds strict non-equilibrium thermodynamic constraints, ensuring the thermodynamic consistency of the coupling process from the bottom layer. Experimental validation shows that the energy balance error does not exceed 2.3%, the mean absolute temperature prediction error does not exceed 0.8°C, and the framework possesses excellent numerical stability and computational efficiency, effectively overcoming the bottlenecks of traditional cross-scale coupling methods in physical consistency and simulation accuracy.

Second, district wind fields significantly influence indoor thermal comfort and system entropy production by regulating convective heat transfer intensity and radiation heat gain distribution. Application case validation indicates that optimizing the wind field can effectively weaken cross-scale energy transfer, reducing the indoor average temperature by 1.8°C; simultaneously, it suppresses turbulence shear and local thermal flux concentration, reducing irreversible energy loss, and lowering the system total entropy production rate by 20.7%; energy efficiency is synchronously improved, with the target building's air-conditioning energy consumption reduced by 17.5%, achieving synergistic optimization of indoor thermal comfort and low-carbon energy saving.

Third, global uncertainty analysis based on Sobol indices shows that the computational fluid dynamics turbulence model constants are the key factors affecting the reliability of simulation results, with a contribution ratio close to 40%. This finding clearly identifies the core direction for subsequent model optimization and provides a definite theoretical and technical basis for further improving simulation accuracy through adaptive calibration of turbulence model parameters.

ACKNOWLEDGMENT

The paper is funded by Soft Science Project of Henan Province (Grant No.: 242400410262;252400410248); Hunan Natural Science Foundation (Grant No.: 2022JJ40875); Doctoral Research Start-Up Fund Project of Nanyang Institute of Technology (Grant No.: NGBJ-2024-21; NGBJ-2024-22); Interdisciplinary Science Research Project of Nanyang University of Technology (Grant No.: 25NGJY029).

REFERENCES

[1] Ahmadizadeh, O., Vakilinezhad, R. (2025). Assessing the impact of PV facades on neighborhood microclimate, outdoor thermal comfort, and energy efficiency in hot climates, case study of Shiraz. Architectural Engineering and Design Management, 1-28. https://doi.org/10.1080/17452007.2025.2456770

[2] Zheng, J., Zhang, H., Liu, Z., Zheng, B. (2024). Research on microclimate performance simulation application and scheme optimization in traditional neighborhood renewal—A case study of Donghuali District, Foshan City. Sustainability, 16(5): 1899. https://doi.org/10.3390/su16051899

[3] Elbondira, T.A., Tokimatsu, K., Asawa, T., Ibrahim, M.G. (2021). Impact of neighborhood spatial characteristics on the microclimate in a hot arid climate–A field based study. Sustainable Cities and Society, 75: 103273. https://doi.org/10.1016/j.scs.2021.103273

[4] Jiang, H., Guo, X., Song, J., Chen, J., Yang, C., Hong, W. (2025). Self-adaptive integration of photothermal conversion and storage via fly ash nanocomposites with biomimetic broccoli-like structure. Journal of Building Engineering, 112: 113719. https://doi.org/10.1016/j.jobe.2025.113719

[5] Sansaniwal, S.K., Mathur, J., Mathur, S. (2022). Review of practices for human thermal comfort in buildings: Present and future perspectives. International Journal of Ambient Energy, 43(1): 2097-2123. https://doi.org/10.1080/01430750.2020.1725629

[6] Antonio, G., Stefano, A., Vincenzo, S. (2025).

Renovation of a historic building respecting the preservation of cultural heritage improving the energy efficiency. International Journal of Computational Methods and Experimental Measurements, 13(3): 641-650. https://doi.org/10.56578/ijcmem130313

[7] Haldar, S., Bhandari, P., Chakraborty, S. (2017). Emergent Scenario in first and second order non-equilibrium thermodynamics and stability analysis. Annals of Physics, 387: 203-212. https://doi.org/10.1016/j.aop.2017.10.013

[8] Katagiri, S. (2018). Non-equilibrium thermodynamics as gauge fixing. Progress of Theoretical and Experimental Physics, 2018(9): 093A02. https://doi.org/10.1093/ptep/pty102

[9] Cao, J., Jiang, G., Ye, N., Qin, Y., Ji, X., Feng, X., Lu, X. (2023). Heterogeneous consecutive reaction kinetics of direct oxidation of H2 to H2O2: Effect and regulation of confined mass transfer. Chemical Engineering Journal, 455: 140111. https://doi.org/10.1016/j.cej.2022.140111

[10] Farmany, A. (2012). Generalized thermodynamics uncertainty and (anti) de Sitter space. Astrophysics and Space Science, 338(2): 401-403. https://doi.org/10.1007/s10509-011-0953-x

[11] Dutta, A., Gangopadhyay, S. (2016). Thermodynamics of black holes and the symmetric generalized uncertainty principle. International Journal of Theoretical Physics, 55(6): 2746-2754. https://doi.org/10.1007/s10773-015-2907-5

[12] Santillán, M., Qian, H. (2011). Irreversible thermodynamics in multiscale stochastic dynamical systems. Physical Review E—Statistical, Nonlinear, and Soft Matter Physics, 83(4): 041130. https://doi.org/10.1103/PhysRevE.83.041130

[13] Ingargiola, A., Laurence, T., Boutelle, R., Weiss, S., Michalet, X. (2016). Photon-HDF5: An open file format for timestamp-based single-molecule fluorescence experiments. Biophysical Journal, 110(1): 26-33. https://doi.org/10.1016/j.bpj.2015.11.013

[14] Könnecke, M., Akeroyd, F.A., Bernstein, H.J., Brewster, A.S., Campbell, S.I., Clausen, B., Wuttke, J. (2015). The NeXus data format. Applied Crystallography, 48(1): 301-305. https://doi.org/10.1107/S1600576714027575

[15] Garcia, R.V., Pardal, P.C.P.M., Kuga, H.K., Zanardi, M.C. (2019). Nonlinear filtering for sequential spacecraft attitude estimation with real data: Cubature Kalman Filter, Unscented Kalman Filter and Extended Kalman Filter. Advances in Space Research, 63(2): 1038-1050. https://doi.org/10.1016/j.asr.2018.10.003

[16] Liu, H., Hu, F., Su, J., Wei, X., Qin, R. (2020). Comparisons on Kalman-filter-based dynamic state estimation algorithms of power systems. IEEE Access, 8: 51035-51043. https://doi.org/10.1109/ACCESS.2020.2979735

[17] Ghaznavi, A., Saberioon, M., Brom, J., Itzerott, S. (2024). Comparative performance analysis of simple U-Net, residual attention U-Net, and VGG16-U-Net for inventory inland water bodies. Applied Computing and Geosciences, 21: 100150. https://doi.org/10.1016/j.acags.2023.100150

[18] Douglas, L., Bhattacharjee, R., Fuhrman, J., Drukker, K., Hu, Q., Edwards, A., Giger, M. (2023). U-Net breast lesion segmentations for breast dynamic contrast-enhanced magnetic resonance imaging. Journal of Medical Imaging, 10(6): 064502. https://doi.org/10.1117/1.JMI.10.6.064502